Fabrication of one-dimensional Bi_2WO_6/$CuBi_2O_4$ heterojunction nanofiber and its photocatalytic degradation property

Pingping Teng [a], Zhiang Li [a], Shuai Gao [a,**], Kang Li [b], Mark Bowkett [b], Nigel Copner [b], Zhihai Liu [a,*], Xinghua Yang [a]

[a] *Key Laboratory of In-Fiber Integrated Optics, Ministry of Education, College of Physics and Optoelectronic Engineering, Harbin Engineering University, Harbin, 150001, China*

[b] *Wireless & Optoelectronics Research & Innovation Centre, Faculty of Computing, Engineering & Science, University of South Wales, Wales, CF37 1DL, UK*

Abstract

In this paper, electrospinning method was used to prepare a one-dimensional nanostructured copper bismuthate- bismuth tungstate photocatalyst. The bismuth tungstate nanosheet structure was prepared by solvothermal method, and the copper bismuthate-bismuth tungstate precursor nanofibers were prepared by electrospinning using the doping method. The one-dimensional copper bismuthate-bismuth tungstate nanofiber structure was prepared by the high-temperature decomposition. The results show that the diameter of the bismuth tungstate and copper bismuthate nanofibers is about 280 nm, with continuous and regular fiber morphology. The fibers are composed of semiconductor nano-heterojunction and show good photocatalytic degradation efficiency for tetracycline hydrochloride. After 120 min of illumination, the degradation efficiency is greater than 90%, and it can be recycled and reused. The photocatalytic mechanism analysis showed that the energy band structure of the copper bismuthate-bismuth tungstate nano-semiconductor fiber was a Z-type heterojunction, and the free radical capture experiment showed that h^+ and $\bullet O^{2-}$ were main groups involved in oxidation reaction. The structure of high specific surface area of the nanofibers will improve the separation of photo-generated electrons and holes, and the experiment results show it has good performance of photocatalytic.

1. Introduction

The living environment, especially the air and water pollution, has been paid much attention. A large number of organic substances, such as pesticides, plastics, antibiotics, dyes, etc., cause serious pollution to the environment, and then seriously affect human health [1−5]. In particular, the governance of soil, air and water play important role in the environment protection [6−10]. Among them, for the prosperity and development of mankind, effective treatment of water pollution has become a major issue that people need to solve urgently [11−13]. Especially, the photocatalytic method has been widely used in the field of environmental pollution degradation because of its environmental friendliness and low cost. As a green photocatalyst, semiconductor nanomaterials have important application prospects in solving global problems such as pollutant degradation and energy shortages [14−18]. Bismuth-based semiconductor materials have the advantages of narrow band gap width, suitable energy band position, higher physical and chemical stability, and low cost. They are used in pollutant degradation, photocatalytic water splitting, and photocatalytic CO_2 reduction [19,20]. In particular, $CuBi_2O_4$ (CBO) is p-type semiconductor with a relatively narrow band gap (about 1.6 eV). $CuBi_2O_4$ is a semiconductor material with a spinel structure [21−23]. It consists of independent CuO_4 faces along the *c* axis to form a staggered collinear "chain", and is connected by BiO_4 units to form a spinel structure. It has been widely used in the fields of organic synthesis and photocatalytic sterilization, and presents a good development prospect. However, the photo-generated electrons and holes of the single-component bis- muth-based semiconductor materials are easily recombined, resulting in low quantum efficiency, thereby reducing their photocatalytic activity. Normally, constructing a heterojunction can effectively improve the efficiency of electron-hole separation. The $CuBi_2O_4$ has great potential to form a Z-scheme heterojunction with many other semiconductor materials such as WO_3, g-C_3N_4, and CuO. Besides, Bi_2WO_6 (BWO) is another Bi-based photocatalyst with potential application with a
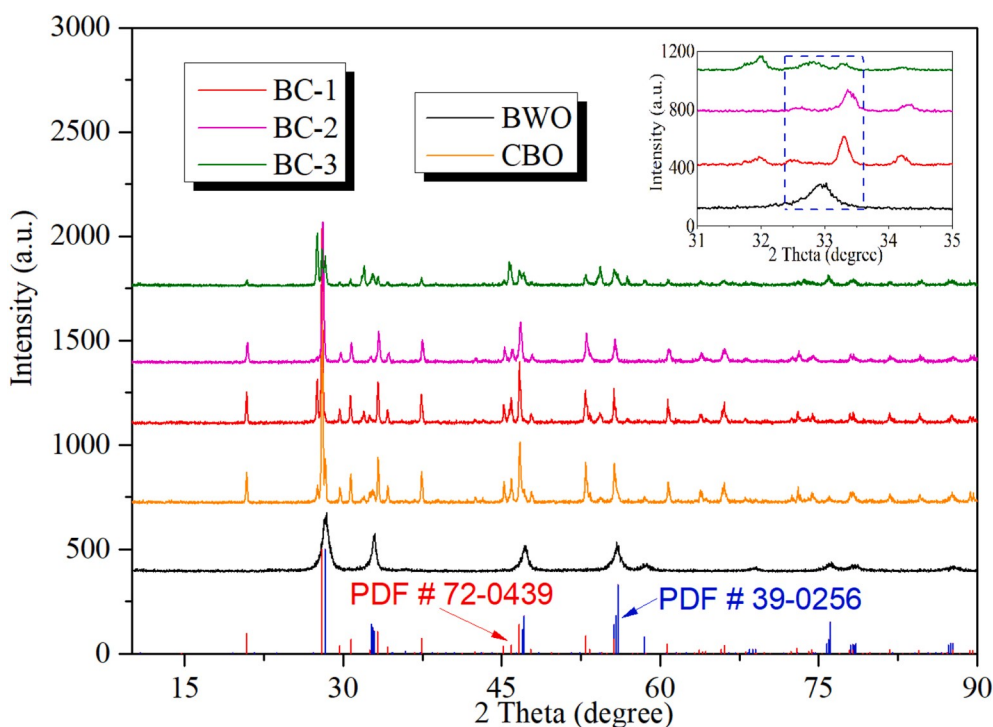

Fig. 1. X-ray powder diffraction pattern of different ratio BWO-CBO samples, illustration is partial enlargement.

sandwich slice structure of WO_6-$(Bi_2O_2)_{2+}$. The band gap is about 2.8 eV and the valence band (VB) position is about 3.2 eV vs. NHE [24,25]. This means it can form Z-scheme heterojunction with $CuBi_2O_4$ to drive electrons with reduction potential in the conduction band (CB) of $CuBi_2O_4$ and form holes with oxidation potential in the VB of Bi_2WO_6. On the other hand, one-dimensional nanomaterials have a large specific surface area and a large aspect ratio [26−28]. At the same time, their surface is allowed to be modified simply, which has great application value in the field of photocatalysis. These one-dimensional nanomaterials can be obtained by methods such as electrospinning, chemical synthesis, and template self-assembly. Among them, the electrospinning method is a simple and effective method for preparing one-dimensional nanomaterials [29−32]. Compared with the zero-dimensional nano-photocatalytic material, due to its fibrous morphology, the one-dimensional nanomaterial prepared by the electrospinning method can effectively overcome the agglomeration between particles in the photocatalytic reaction. Because the fibrous material has good dispersibility and large specific surface area, it can fully contact with the reactant and improve the photocatalytic activity and the repeated utilization [33,34].

In this paper, solvothermal technology and electrospinning technology are combined to prepare one-dimensional $CuBi_2O_4$−Bi_2WO_6 fiber with Z-scheme heterojunction. The Bi_2WO_6 nanoparticles are synthesized by the solvothermal method are mixed with the $CuBi_2O_4$ precursor solution, electrospinning is performed, and finally the heat treatment is performed to obtain a copper bismuthate-bismuth tungstate heterojunction.

2. Experimental section

2.1. Solvothermal synthesis of Bi$_2$WO$_6$

2.93 g of $Bi(NO_3)_3 \cdot 5(H_2O)$ was added to 30 mL of glacial acetic acid and dissolved by ultrasound. 0.99 g of Na_2WO_4 was dissolved in 150 mL of deionized water. The $Bi(NO_3)_3$ solution was added to the aqueous solution of Na_2WO_4 and stirred for 30 min. The above-mentioned mixed solution was equally divided into three parts, and respectively added to

three 100 mL stainless steel autoclaves and reacted at 180 °C for 24 h. Then, the reactor was cooled to room temperature. The solution was centrifuged and washed with deionized water for 3 times, and finally washed with ethanol once, and dried at 80 °C for 5 h. Finally, light green Bi_2WO_6 nanopowder was obtained.

2.2. Preparation of Bi$_2$WO$_6$−CuBi$_2$O$_4$ heterojunction fiber

8.4 g of PVP (Mw=1300000) was added to a mixed solution of 24 g of glacial acetic acid, 30 g of absolute ethanol and 54 g of DMF. The solution was stirred at room temperature for 12 h. 3.615 g of $Cu(NO_3)_2 \cdot 3H_2O$ and 14.515 g of $Bi(NO_3)_3 \cdot 5(H_2O)$ were added to the above solution and stirred for 6 h to form a light blue transparent solution. Three parts of the above solutions were weighed separately with each with a mass of 33.3 g, and 0.5 g, 2 g, 3.4 g of BWO powder were added to the three solutions and stirred for 3 h. The above solution was placed in a 5 mL syringe, and electrospinning was performed under a high voltage of 10 kV. The distance between the needle and the aluminum foil receiving plate was 12 cm. The liquid supply rate was controlled by a syringe pump, and the sampling rate was 0.01 mL/min. The prepared nanofibers were vacuum dried at 50 °C for 5 h. The dried fiber was calcined at 600 °C for 2 h, and the heating rate of the muffle furnace was 1 °C/min. Finally, the Bi_2WO_6−$CuBi_2O_4$ one-dimensional heterojunction fiber with 20%, 50%, and 80% BWO by mass was obtained. The three fiber samples were labeled BC-1, BC-2 and BC-3, respectively.

3. Results and discussion

3.1. Structure characterization of the samples

The crystal structure of the sample prepared by electrostatic spinning is characterized by X-ray powder diffraction (XRD). It can be seen from the XRD spectrum (Fig. 1), and the diffraction peak of BWO corresponds to the PDF#39−0256. 28.3°, 32.8°, 47.1°, 55.8° and 58.5° respectively correspond to (131), (200), (202), (331), and (262) diffraction surfaces. The main diffraction peaks of CBO such as 20.9, 28.0, 30.8, 33.3, 37.5, 46.7, 53.0, 55.7 correspond to (200), (211), (002), (310), (202), (411),
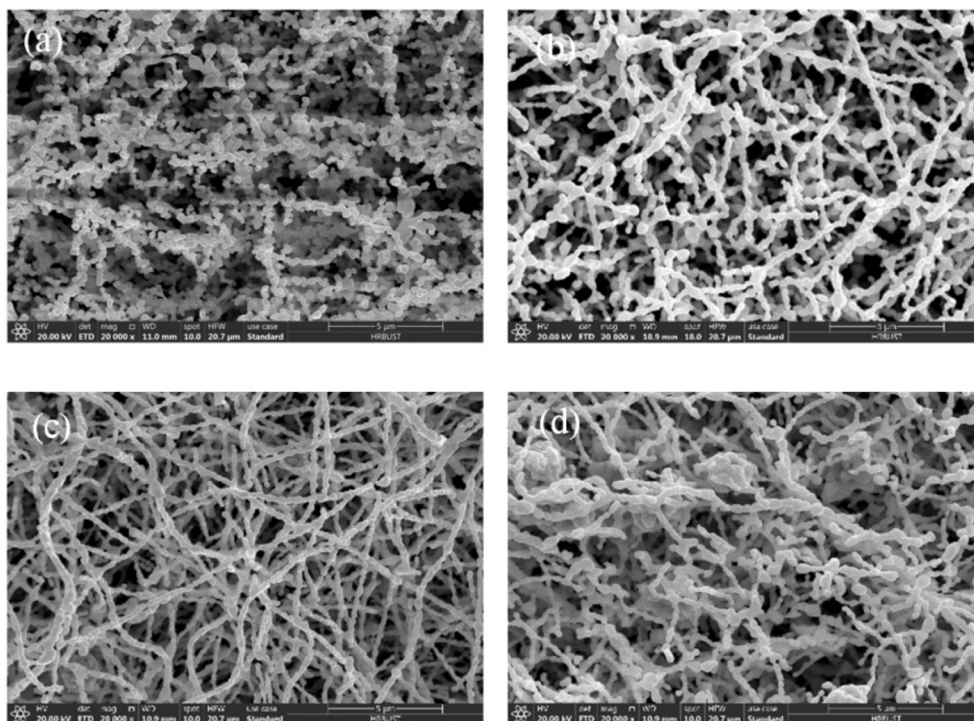
Fig. 2. SEM photos of catalyst samples annealed at high temperature (a) CBO (b) BC-1 (c) BC-2 (d) BC-3.
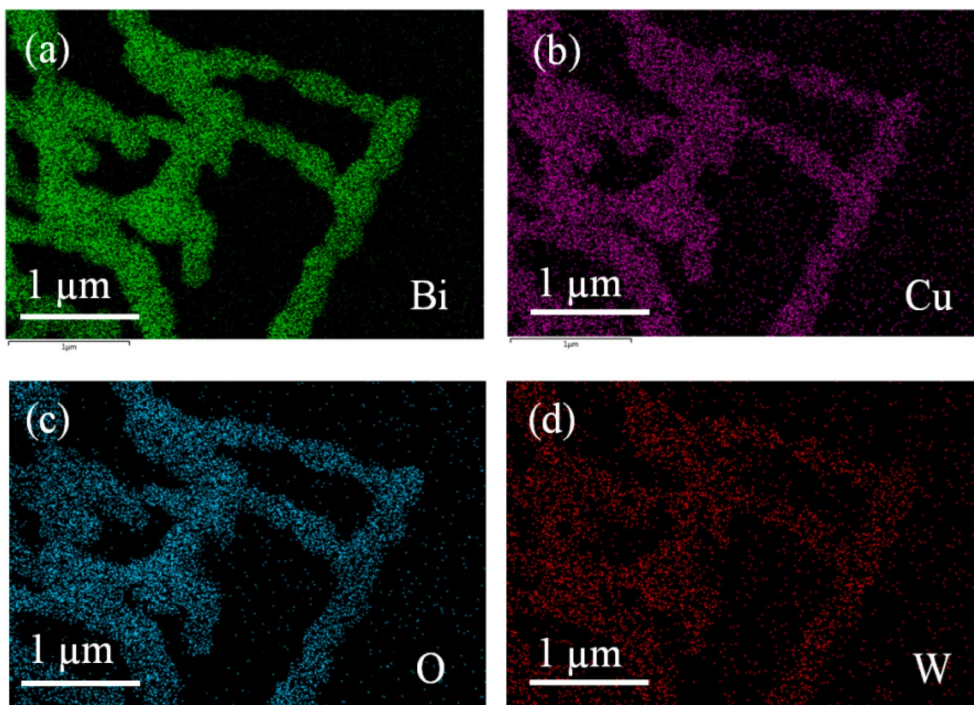

Fig. 3. Surface scan elemental analysis of BC-2 sample (a) Bi (b) Cu (c) O (d) W.

(213), (332) diffraction surfaces according to PDF # 72−0439. In the BWO-CBO heterojunction sample, the diffraction peak of Kusachiite type CBO can be observed. As shown in the illustration of the BC-1, BC-2, BC-3 diffraction curves, with the mass increase of BWO, it can be observed that the strength ratio of the neighborhood of BWO and CBO is gradually increased. The results prove the formation of BWO-CBO heterojunction.

3.2. Morphologies and element distribution

The morphology of the fiber sample prepared by electrospinning is shown in Fig. 2. Fig. 2(a) shows the morphology of CBO samples after high temperature calcination. It can be seen from the figure that there is almost no fiber morphology in the precursor fiber after high temperature reaction. But after adding BWO in the precursor solution, the scanning electron microscope (SEM) micro morphology is obviously different,
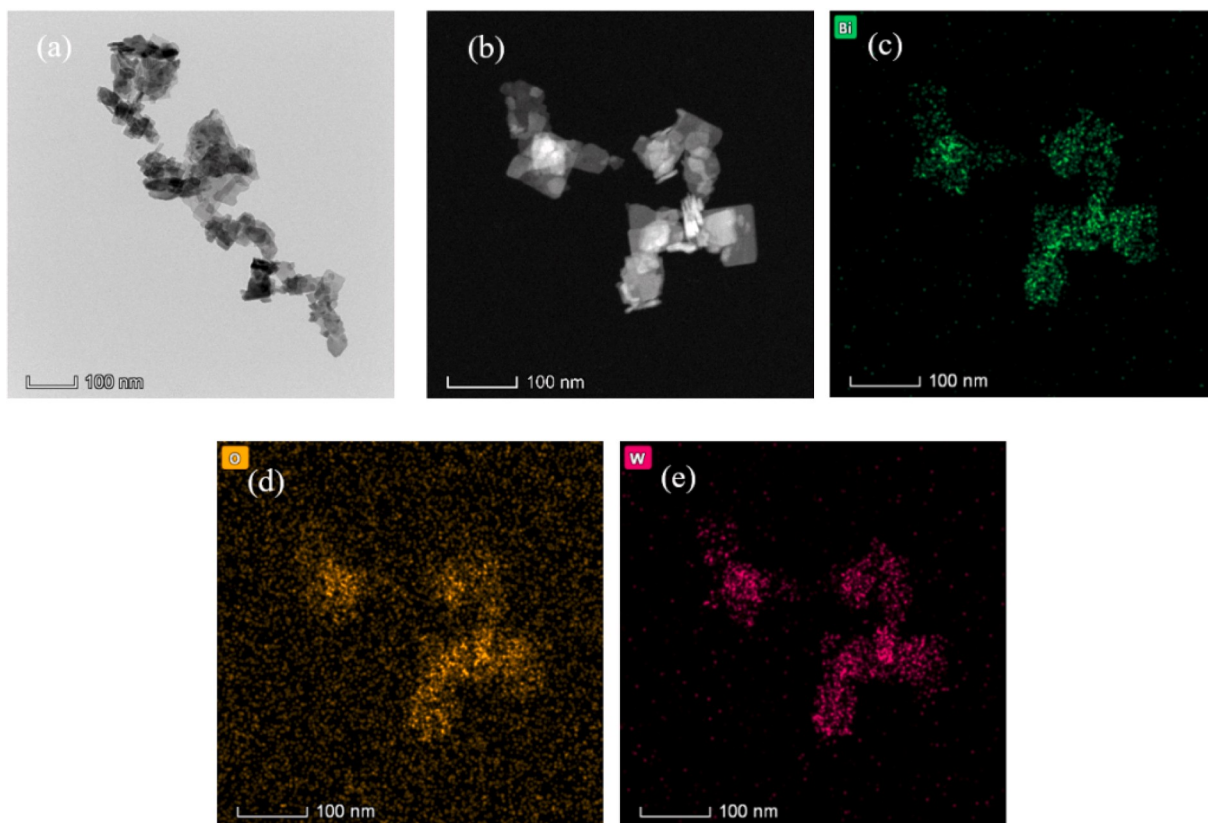
Fig. 4. TEM images of BWO samples (a)solvothermal BWO samples (b)−(e) dark field BWO samples and their element distributions of Bi, W, O.

showing the fiber morphology characteristics. The reason is that the addition of BWO makes the product particles of CBO precursor combine more firmly during the decomposition process, which can explain the heterojunction between CBO and BWO. Fig. 2 (b), Fig. 2 (c) and Fig. 2 (d) correspond to the morphologies of samples with different Bi_2WO_6−$CuBi_2O_4$ mass ratios, respectively. SEM results show that the diameters of the three samples with different BWO concentrations are basically the same after calcination, but the fiber morphologies are different. When BWO concentration is 20%, the fiber is discontinuous. When the concentration reaches 50%, the samples are continuous fibers with a diameter of about 280 nm. However, when the BWO concentration continues to increase to 80%, due to the higher BWO content and higher

solution viscosity, the spinning morphology is poor and the fiber appears discontinuous state. It can be seen that the concentration of BWO has a great influence on the continuity of the fiber. The results show that the optimum doping concentration is 50%.

Fig. 3 shows the distribution of elements in the local morphology of the fiber. In this figure, Fig. 3(a)−(d) correspond to the distribution of Bi, Cu, W and O, respectively. It can be seen from the figure that the four elements are uniformly distributed in the fiber, which indicates that BWO can be uniformly dispersed in CBO precursor when BWO nanoparticles are mixed into CBO precursor and electrospun. At the same time, after spinning and calcinating, the two substances are formed in the fiber, and there is no obvious phase separation. BWO and CBO have a
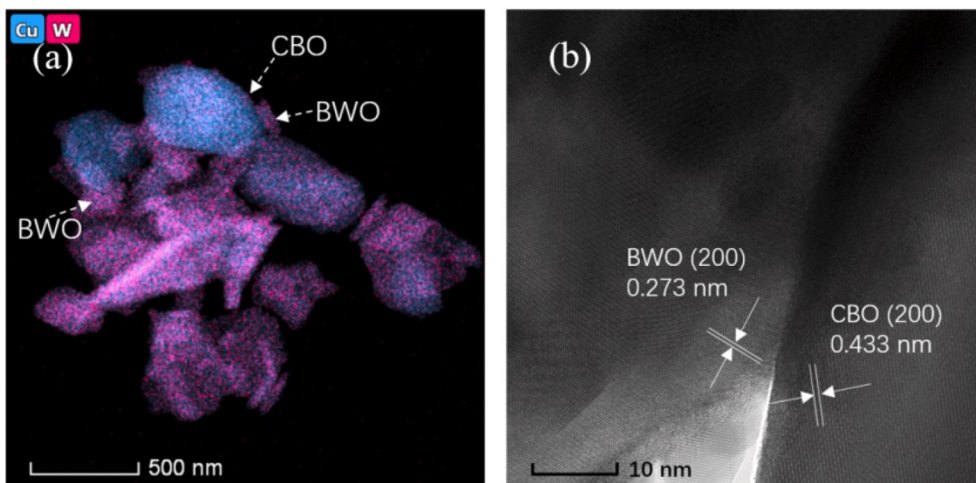

Fig. 5. HRTEM analysis of BC-2 sample with heterojunction semiconductor structure (a) distribution of elements Cu and W in heterojunction (b) lattice structure of heterojunction high resolution transmission electron microscope.
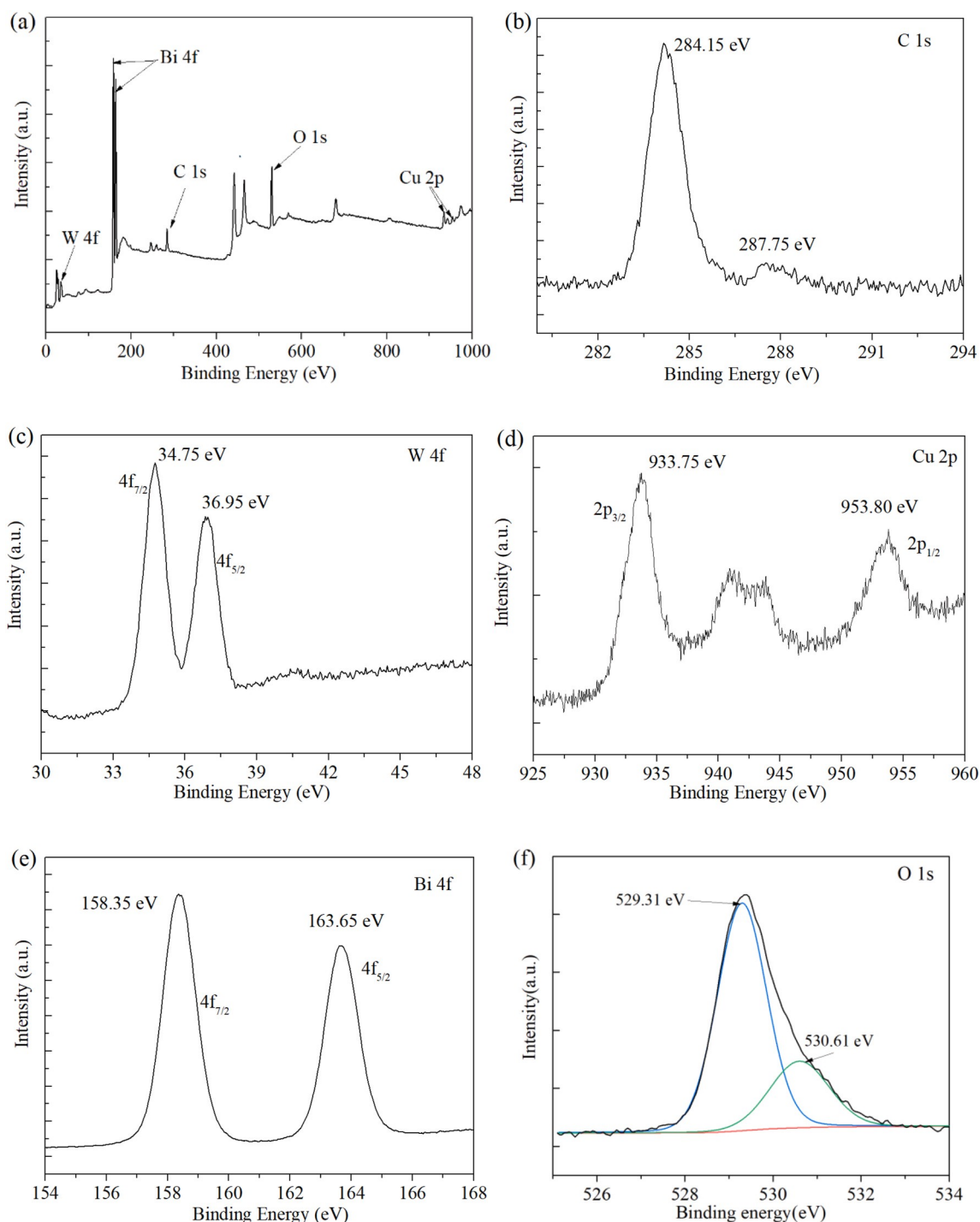
Fig. 6. X-ray photoelectron spectroscopy (a) full spectrum (b)−(f) C 1s, W 4f, Cu 2p, Bi 4f, O 1s fine spectrum of BC-2 sample.

uniform contact macroscopically. This will help to form a large number of heterojunctions.

In order to further determine the distribution of BWO in the fiber and the formation of heterojunction with CBO, the BWO prepared by solvothermal method and the BC-2 samples were characterized by transmission electron microscopy (TEM). Fig. 4 shows the TEM morphology of BWO. From Fig. 4(a), we can observe the BWO prepared by solvothermal method is sheet-like nanostructure with diameters of about 20−40 nm. According to the element distribution in the dark field shown in Fig. 4(b)−(e), Bi, W and O are evenly distributed in the nanoparticles.

High resolution transmission electron microscope (HRTEM) images of BC-2 sample after ultrasonic dispersion are shown in Fig. 5. The element distribution in Fig. 5(a) shows that Cu and W are distributed in different nanoparticles, the area of Cu distribution corresponds to CBO particles, and the area of W distribution corresponds to BWO nanosheets. The contact part between BWO and CBO can be observed. As shown by the high-resolution transmission microscope photo in Fig. 5 (b), two different lattice fingerprints can be observed at the junction, with gaps of 0.273 nm and 0.433 nm, respectively. These two parameters correspond to (200) crystal plane of CBO and (200) crystal plane of BWO. This can prove the production of BWO-CBO heterojunction in the fiber.
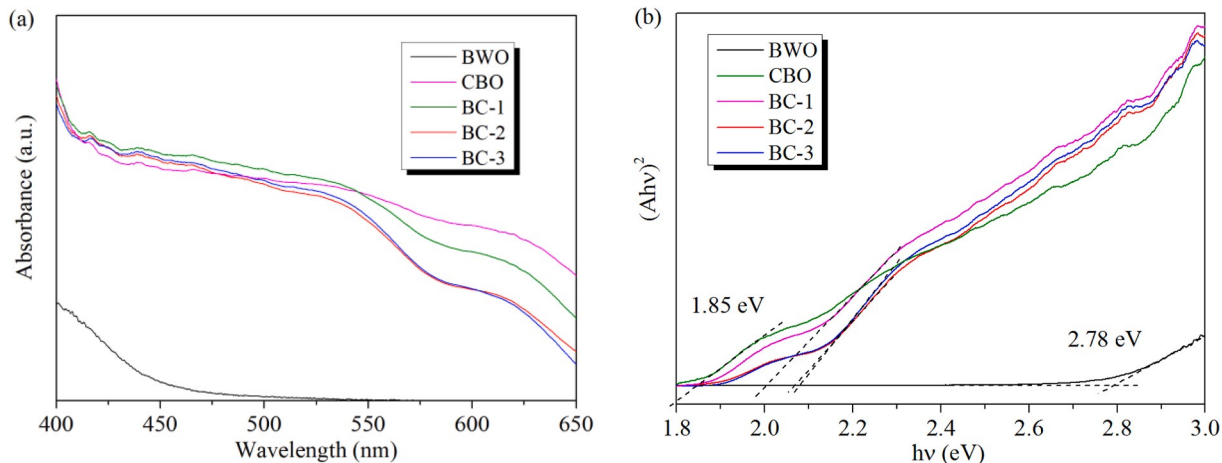
Fig. 7. (a) UV−Vis diffuse reflectance spectra of BWO, CBO, BC-1, BC-2 and BC-3 samples (b) $h\nu$-$(\alpha h\nu)^2$ curves of the samples.

3.3. Chemical composition and electronic state of photocatalyst

In order to determine the chemical composition and electronic state of the fiber surface, the BC-2 sample was analyzed by X-ray photoelectron spectroscopy (as shown in Fig. 6). Fig. 6(a) shows the whole XPS scanning line. It can be seen that the fiber surface contains W, Bi, Cu and O elements. Fig. 6(b) shows the carbon element in the test process to calibrate the binding energy. Fig. 6(c)−(f) shows the high resolution XPS spectra of various elements. The 34.75 eV and 36.95 eV peaks of W4f in Fig. 6(c) correspond to the binding energies of W $4f_{7/2}$ and W $4f_{5/2}$ in BWO, respectively [35]. In Fig. 6(d), the orbital and spin motion of Cu 2p electrons are coupled, and the orbital energy levels are split, which are 933.75 eV and 953.80 eV, respectively, and are attributed to Cu $2p_{3/2}$ and Cu $2p_{1/2}$ of Cu in CBO [36]. As shown in Fig. 6(e), the two binding energy peaks of 158.35 eV and 163.65 eV of Bi 4f orbital correspond to Bi $4f_{7/2}$ and Bi $4f_{5/2}$ [34] respectively, which proves the existence of Bi^{3+} valence state in CBO material. In Fig. 6(f), the XPS spectrum of O 1s, there is a shoulder peak near 530 eV. Two XPS peak positions were obtained by sub peak fitting. They are located at 529.31eV and 530.60 eV, respectively. The peak of 529.31 eV corresponds to lattice oxygen, and 530.60 eV corresponds to oxygen vacancies. The oxygen vacancies come from the surface absorption of oxygen as well as −OH from the residual energy gap [37,38]. The above results further indicate that the existing forms of W, Bi, Cu and O are CBO and BWO.

In order to characterize the effect of CBO on the absorption characteristics of BWO in fiber samples, the optical absorption characteristics of pure BWO, CBO and BC-1, BC-2 and BC-3 samples were characterized by UV−Vis diffuse reflectance spectroscopy. As shown in Fig. 7(a), the absorption band edge of pure BWO nanosheets is close to the short wavelength direction of the visible region, and is about 450 nm, indicating that BWO has a broad band gap, while the composites absorbed a large proportion of the visible-light. For the BC-1, BC-2 and BC-3 samples, the absorption band edge has a significant red shift because of the heterojunction forming, which makes the absorption of the sample expand significantly in the visible region. This will make the photocatalyst more beneficial to the use of visible light. The band gap energy of the sample is calculated by the following:

$$\alpha h\nu = A(h\nu - E_g)^{1/2}$$

here α, E_g, A, h, v are molar absorption coefficient, semiconductor optical band gap, proportional constant, Planck constant and incident photon frequency respectively [34]. From $h\nu$-$(\alpha h\nu)^2$ curve, as shown in Fig. 7(b), the sample band gap can be estimated by the intersection of the tangent and the x-axis. It can be seen from the figure that the band gap of BWO is about 2.78 eV, while that of CBO has a significantly narrowed width of 1.85 eV. In addition, with the formation of heterojunctions, the band gaps of BC-1, BC-2 and BC-3 are 1.99 eV, 2.06 eV and 2.08 eV, respectively. Compared with the BWO, the band gaps of composites are obviously increased. The change of band gap indicates that a heterojunction is formed between CBO and BWO and more photomotivated carries can be obtained in composites because the CBO can provide an easier path for carries generation [39].
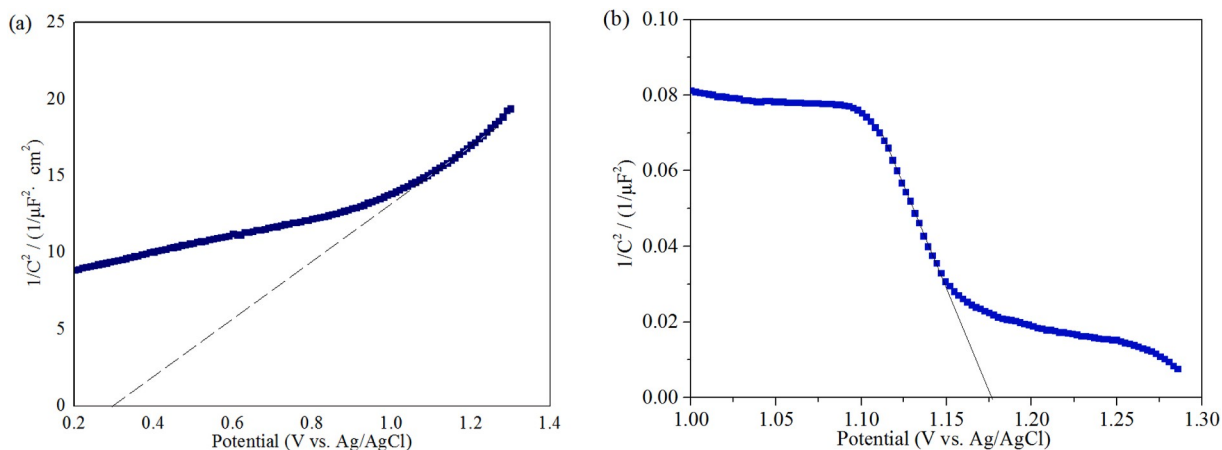

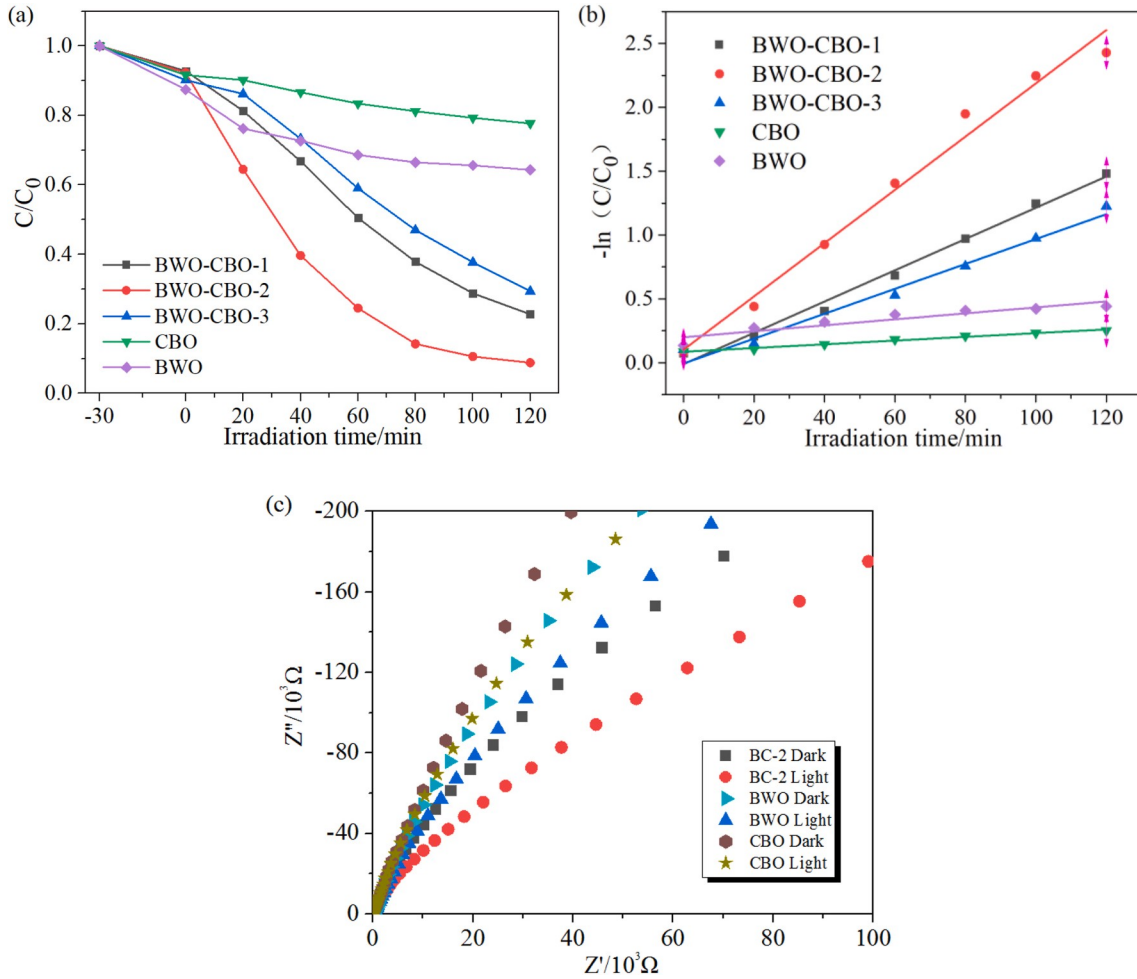**Fig. 8.** Mott-Schottky curve of samples (a) BWO (b) CBO.

Fig. 9. Characterization of photocatalytic degradation of tetracycline hydrochloride (a) Degradation curves of tetracycline hydrochloride by different catalysts of CBO、BWO、BC-1、BC-2、BC-3 (b) Linear fitting diagram of first order kinetics of degradation process of CBO、BWO、BC-1、BC-2、BC-3 (c) Nyquist diagram of electrochemical impedance of CBO, BWO and BC-2 under light and no light.

The Mott-Schottky curves of BWO and CBO are shown in Fig. 8. The intersection of the tangent of the curves and the x-axis is the flat band potential. Because the tangent slope of BWO in Fig. 8(a) is positive [33], it can be seen that BWO is an n-type semiconductor, and its flat band potential is similar to its conduction band potential CB value, corresponding to the Ag/AgCl electrode potential of 0.29 V (converted into standard hydrogen electrode potential of 0.48 V vs. NHE). The tangent slope of CBO in Fig. 8(b) is negative, which indicates that CBO is a p-type semiconductor, and its flat band potential is similar to its valence band potential VB value, corresponding to Ag/AgCl electrode potential of 1.16 V (converted to standard hydrogen electrode potential of 1.36 V vs. NHE). The catalytic activity of photocatalyst is closely related to its band structure. The conduction band bottom potential and valence band top potential can be gotten from the formula [40]:

$$E_{CB} = E_{VB} - E_g$$

E_g is the band gap of CBO or BWO, E_{VB} is the top potential of valence band (VB) and E_{CB} is the bottom potential of conduction band (CB). After calculation, the VB value of BWO is 3.28 eV, and the CB value of CBO is —0.31 eV.

3.4. Catalytic performance of photocatalyst

In the experiment of photocatalytic degradation of organic matter, 150 W xenon lamp was used as the light source. Tetracycline

hydrochloride (TC) was used as the degradation substance, and 20 mg L^{-1} TC solution was prepared. 50 mg of BC-2 was added to 50 mL of the above solution. The catalyst was balanced with TC by magnetic stirring for 30 min in dark environment. Then the solution was irradiated with light source and stirred with magnetic force at the same time. 4 mL of the solution was taken out and centrifuged every 20 min. The absorbance change of the solution at 358 nm was recorded with a spectrophotometer. As shown in Fig. 9(a), the catalytic effect of BWO is slightly better than that of CBO. However, the photodegradation curve showed that the catalytic efficiency of the composite catalyst formed by BWO and CBO was significantly higher than that of the two single components. At 120 min, the degradation rate of 20 mg/L TC solution by BWO was about 30%, and the catalytic degradation rate of BC-1, BC-2 and BC-3 samples reached 78.3%, 91.9% and 71.8%, respectively. The degradation rate of BC-2 is more than three times that of BWO at the same time. The degradation reaction rate was fitted by kinetic rate analysis, and the degradation catalysis was in accordance with Langmuir-Hinshelwood apparent first-order kinetic model [41]:

$$r = dC/dt = kk'C/(1 + k'C)$$

where r is the degradation rate (mg $L^{-1}h^{-1}$), C is the concentration of the degraded product (mg L^{-1}), t is the illumination time (h), k is the reaction rate constant (mg·$L^{-1}h^{-1}$), k' is the adsorption coefficient of degraded products (L·mg^{-1}). Because the initial concentration of degraded products is low, the above equation can be simplified as a first-
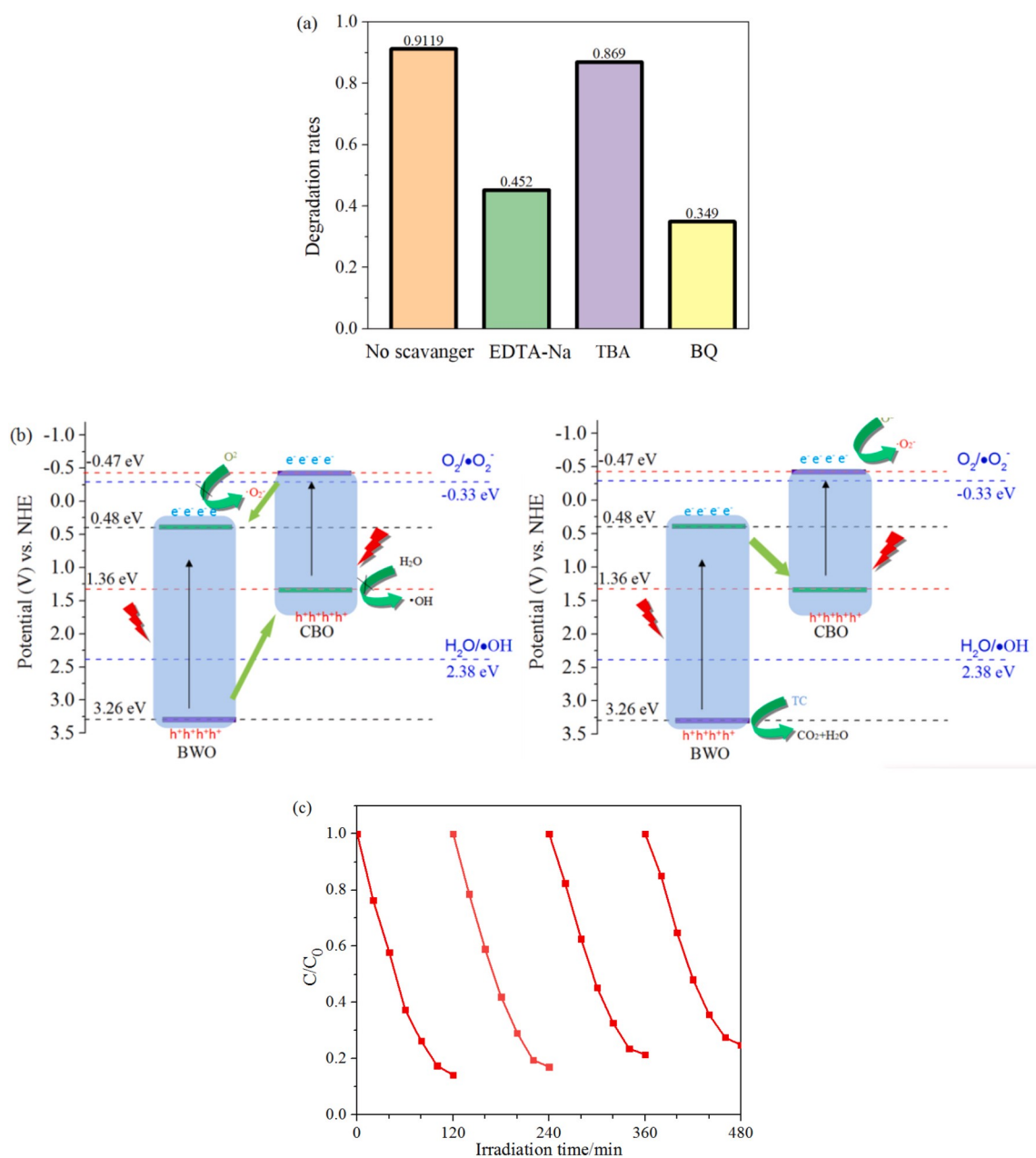
Fig. 10. (a) The effect of different trapping agents on the degradation efficiency of BC-2 (b) the process of photogenerated electron-hole separation, transfer and photocatalytic reaction of CBO and BWO heterojunction under illumination: the type II mechanism (left) and the Z-scheme (right) (c) the cyclic degradation experiment of BC-2.

order model:

$$-(C / C0) = kk't = k_{app}t$$

where C_0 is the concentration of the solution after the adsorption of the photocatalyst reaches the adsorption desorption equilibrium, and Kapp is the apparent first-order rate constant. As shown in Fig. 9(b), the apparent rate constants Kapp of CBO, BWO, BC-1, BC-2 and BC-3 are 0.00146 min^{-1}, 0.00234 min^{-1}, 0.01225 min^{-1}, 0.02087 min^{-1} and 0.00975 min^{-1}, respectively. The catalytic efficiency of BC-2 is 14.3 and 8.9 times higher than that of CBO and BWO, respectively, which indicates that BWO and CBO heterojunction has higher catalytic efficiency, and BC-2 heterojunction has larger contact area. It can be seen that the formation of BWO and CBO composite photocatalyst heterojunction promotes the separation efficiency of photogenerated carriers in the catalytic process, and further improves the catalytic efficiency.

Meanwhile, as shown in Fig. 9(c), the interfacial charge transfer characteristics of the sample were studied by electrochemical impedance spectroscopy (EIS). The arc in the impedance spectrum can reflect the catalytic performance of the catalyst. For the same photocatalyst, through the comparison of impedance spectrum before and after illumination, it is found that the impedance arc radius of each catalyst under illumination is smaller than that without illumination, indicating its essential characteristics as a photocatalyst. In addition, it can be seen from the figure that the impedance arc radius of CBO and BWO is large, and when the heterojunction is formed, the impedance arc radius of cbo-bwo-2 nanofiber becomes significantly smaller, indicating that the interfacial charge transfer performance of cbo-bwo-2 heterojunction is better than that of single component photocatalyst, which is beneficial to improving photocatalytic activity.

3.5. Catalytic mechanism of photocatalyst

The photocatalytic degradation mechanism of BC-2 was studied. The active groups were determined by adding capture agent in photocatalytic reaction, and the types of active groups were determined from the influence of capture agent on degradation efficiency. As shown in Fig. 10(a), Sodium ethylenediaminetetraacetic (Na_2EDTA), Tert butyl alcohol (TBA) and P-benzoquinone (BQ) are used as trapping agents for hole (h^+), hydroxyl radicals ($\cdot OH$), superoxide radicals ($\cdot O_2^-$). When Na_2EDTA, TBA and BQ were added into the degradation solution, the degradation rate of BC-2 to TC reached 45.2%, 86.9% and 34.9% respectively in 120 min. This shows that h^+, $\cdot OH$, $\cdot O_2^-$ has a certain effect on the photodegradation process. In contrast, the addition of h^+, OH and $\cdot O_2^-$ capture significantly reduced the activity of the catalyst, which proved that h^+ and $\cdot O_2^-$ played a major role in photodegradation. In addition, h^+ can not only directly mineralize TC, but also react with water to produce a certain amount of $\cdot OH$ and then mineralize tetracycline hydrochloride.

As shown in Fig. 10(b), there are two possible charge transfer mechanisms of the catalyst, one is the traditional type II mechanism, the other is the Z scheme. If it is type II mechanism (left), for the production of $\cdot O_2^-$, the conduction band position of BWO is 0.48 eV vs. NHE, which is lower than the standard reduction potential of $O_2/\cdot O_2^-$ (-0.33 eV). So the electrons in the BWO band will not reduce the O_2 adsorbed on the surface and change into the $\cdot O_2^-$. If it is Z-scheme mechanism (right), the conduction band electrons generated by BWO transition are transferred to the h^+ of CBO to complete the electron transfer and efficient electron hole separation of the catalyst. At the same time, the h^+ of BWO and the $\cdot O_2^-$ produced by CBO conduction band can directly oxidize organic molecules and decompose them into small molecules to complete the degradation. It can be seen that BWO-CBO heterojunction is a Z-scheme heterojunction. Fig. 10(c) shows the results of reusability of photocatalyst. Four times of centrifugation recycling experiments were carried out on the photocatalyst. After repeated photocatalytic degradation of the same solution, it was found that the photocatalyst could still retain high photocatalytic activity.

4. Conclusion

Copper bismuth-bismuth tungstate photocatalyst with one-dimensional nanostructure was prepared by electrospinning. Bismuth tungstate nanosheets were prepared by solvothermal method, and doped into the precursor solution of copper bismuth. Polymer inorganic salt nanofibers were prepared by electrospinning with PVP polymer system. One dimensional nanofiber was obtained after high temperature decomposition. XRD results show that the oxide prepared by slow decomposition at 600 ˚C has obvious diffraction characteristic peaks. Combined with XPS electronic valence, the fiber is composed of bismuth tungstate and copper bismuth. SEM results show that the fiber has continuous and regular morphology, and its diameter is about 280 nm. Element distribution and high-resolution transmission electron microscopy analysis showed that bismuth tungstate and copper bismuth oxide formed semiconductor nano heterojunction. By adjusting the mass ratio of the two composite oxides, the material showed good photocatalytic degradation efficiency for tetracycline hydrochloride. After 120 min of illumination, the degradation efficiency is more than 90%, and can be recycled stably. The energy band structure of the nanofibers was determined to be Z-type heterojunction by spectroscopic and electrochemical analysis. The analysis of capture mechanism of photocatalysis free radical shows that hole and oxygen free radical participate in oxidation reaction as main groups. In the process of photocatalysis, the electrons in the conduction band of copper bismuth oxide flow to the valence band of bismuth tungstate. Combined with the structural characteristics of high specific surface area of nanofibers, the electron hole separation is promoted. A large number of holes were generated in the valence band of bismuth tungstate, and a large number of $\cdot O_2^-$ were generated in the conduction band of copper bismuth, and the photocatalyst showed good photocatalytic performance.

CRediT authorship contribution statement

Pingping Teng: Conceptualization, Methodology, Software, Investigation, Writing − original draft. **Zhiang Li:** Validation, Resources, Data curation, Writing − review & editing, Supervision. **Shuai Gao:** Formal analysis, Data curation, Visualization, Writing − original draft. **Kang Li:** Writing − review & editing, Supervision. **Mark Bowkett:** Writing − review & editing, Supervision. **Nigel Copner:** Writing − review & editing, Supervision. **Zhihai Liu:** Writing − review & editing, Validation. **Xinghua Yang:** Writing − review & editing, Supervision.

Declaration of competing interest

The authors declare that they have no known competing financial interests or personal relationships that could have appeared to influence the work reported in this paper.

Acknowledgments

References

[1] M. Ashraf, I. Khan, M. Usman, A. Khan, S.S. Shah, A.Z. Khan, K. Saeed, M. Yaseen, M.F. Ehsan, M.N. Tahir, N. Ullah, Hematite and magnetite nanostructures for green and sustainable energy harnessing and environmental pollution control: a review, Chem. Res. Toxicol. 33 (2020) 1292−1311.

[2] Y. Ye, Y. Zhang, Y. Zhao, Y. Ren, X. Ren, Sensitivity influencing factors during pesticide residue detection research via a terahertz metasensor, Opt Express 29 (2021) 15255−15268.

[3] A. Mukherjee, A. Satish, A. Mullick, J. Rapolu, S. Moulik, A. Roy, A.K. Ghosh, Paradigm shift toward developing a zero liquid discharge strategy for dye-contaminated water streams: a green and sustainable approach using hydrodynamic cavitation and vacuum membrane distillation, ACS Sustain. Chem. Eng. 9 (2021) 6707−6719.

[4] M.S. Bank, P.W. Swarzenski, C.M. Duarte, M.C. Rillig, A.A. Koelmans, M. Metian, S. Wright, J.F. Provencher, M. Sanden, A. Jordaan, M. Wagner, M. Thiel, Y.S. Ok, Global plastic pollution observation system to aid policy, Environ. Sci. Technol. 55 (2021) 7770−7775.

[5] Y. Feng, X. Chen, Y. Li, H. Zhao, L. Xiang, H. Li, Q. Cai, N. Feng, C. Mo, M. Wong, A visual leaf zymography technique for the in situ examination of plant enzyme activity under the stress of environmental pollution, J. Agric. Food Chem. 68 (2020) 14015−14024.

[6] Z. Zhao, T. Nie, Z. Yang, W. Zhou, The role of soil components in the sorption of tetracycline and heavy metals in soils, RSC Adv. 8 (2018) 32178−32187.

[7] Y. Wang, M. Makkee, The influence of CO2 on NO reduction into N2 over reduced ceria-based catalyst, Appl. Catal. B Environ. 221 (2018) 196−205.

[8] R. Kim, J. Yoon, T. Kim, J. Yang, G. Owens, K. Kim, Bioavailability of heavy metals in soils: definitions and practical implementation-a critical review, Environ. Geochem. Health 37 (2015) 1041−1061.

[9] R. Zheng, X. Feng, W. Zou, R. Wang, D. Yang, W. Wei, S. Li, H. Chen, Converting loess into zeolite for heavy metal polluted soil remediation based on "soil for soil-remediation" strategy, J. Hazard Mater. 412 (2021) 125199.

[10] A. Rafiq, M. Ikram, S. Ali, F. Niaz, M. Khan, Q. Khan, M. Maqbool, Photocatalytic degradation of dyes using semiconductor photocatalysts to clean industrial water pollution, J. Ind. Eng. Chem. 97 (2021) 111−128.

[11] O. Jovanovic, C.F. Amábile-Cuevas, C. Shang, C. Wang, K.W. Ngai, What water professionals should know about antibiotics and antibiotic resistance: an overview, ACS EST Water 1 (2021) 1334−1351.

[12] T. Zhang, J. Liu, F. Zhou, S. Zhou, J. Wu, D. Chen, Q. Xu, J. Lu, Polymer-coated Fe2O3 nanoparticles for photocatalytic degradation of organic materials and antibiotics in water, ACS Appl. Nano Mater. 3 (2020) 9200−9208.

[13] S. Li, S. Zhou, H. Xu, L. Xiao, Y. Wang, H. Shen, H. Wang, Q. Yuan, Luminescent properties and sensing performance of a carbon quantum dot encapsulated mesoporous silica/polyacrylonitrile electrospun nanofibrous membrane, J. Mater. Sci. 51 (2016) 6801−6811.

[14] S.L. Qu, X. Yuan, Y. Li, X.Y. Li, X.J. Zhou, X.G. Xue, K. Zhang, J. Xua, C.L. Yuan, Aqueous synthesis of composition-tuned defects in CuInSe2 nanocrystals for enhanced visible-light photocatalytic H2 evolution, Nanoscale Adv. 3 (2021) 2334.

[15] P. Zhou, J.G. Yu, M.T. Jaroniec, All-solid-state Z-scheme photocatalytic systems, Adv. Mater. 26 (2014) 4920−4935.

[16] H.L. Wang, L.S. Zhang, Z.G. Chen, J.Q. Hu, S.J. Li, Z.H. Wang, J.S. Liu, X.C. Wang, Semiconductor heterojunction photocatalysts: design, construction, and photocatalytic performance, Chem. Soc. Rev. 43 (2014) 5234−5244.

[17] Q. Jiang, M.Z. Liu, C.L. Shao, X.W. Li, H.Y. Liu, X.H. Li, Y.C. Liu, Nitrogen doping polyvinylpyrrolidone-based carbon nanofibers via pyrolysis of g-C_3N_4 with tunable chemical states and capacitive energy storage, Electrochim. Acta 330 (2020) 135212.

[18] F. Xu, B.C. Zhu, B. Cheng, J. Yu, J.S. Xu, 1D/2D TiO_2/MoS_2 hybrid nanostructures for enhanced photocatalytic CO_2 reduction, Adv. Opt. Mater. 6 (2018) 1800911.

[19] R. Tao, X.H. Li, X.W. Li, S. Liu, C.L. Shao, Y.C. Liu, Discrete heterojunction nanofibers of $BiFeO_3$/Bi_2WO_6: novel architecture for effective charge separation and enhanced photocatalytic performance, J. Colloid Interface Sci. 572 (2020) 257−268.

[20] T. Gao, Z. Chen, Q.L. Huang, F. Niu, X.N. Huang, L.S. Qin, Y.X. Huang, A review: preparation of bismuth ferrite nanoparticles and its applications in visible-light-induced photocatalyses, Rev. Adv. Mater. Sci. 40 (2015) 97−109.

[21] N.T. Hahn, V.C. Holmberg, B.A. Korgel, C.B.J. Mullins, Electrochemical synthesis and characterization of p-$CuBi_2O_4$ thin film photocathodes, J. Phys. Chem. C 116 (2012) 6459−6466.

[22] T. Arai, Y. Konishi, Y. Lwasaki, H. Sugihara, K. Sayama, High-throughput screening using porous photoelectrode for the development of visible-light-responsive semiconductors, J. Comb. Chem. 9 (2007) 574−581.

[23] S.P. Berglund, F.F. Abdi, P. Bogdanoff, A. Chemseddine, D. Friedrich, R.V. Krol, Comprehensive evaluation of $CuBi_2O_4$ as a photocathode material of photoelectrochemical water splitting, Chem. Mater. 28 (2016) 4231−4242.

[24] J. Zhang, J.Y. Xin, C.L. Shao, X.H. Li, X.W. Li, S. Liu, Y.C. Liu, Direct Z-scheme heterostructure of p-$CuAl_2O_4$/n-Bi_2WO_6 composite nanofibers for efficient overall water splitting and photodegradation, J. Colloid Interface Sci. 550 (2019) 170−179.

[25] R. Tao, C.C. Zhao, C.L. Shao, X.H. Li, X.W. Li, J. Zhang, S. Yang, Y.C. Liu, Bi_2WO_6/$ZnFe_2O_4$ heterostructures nanofibers: enhanced visible-light photocatalytic activity and magnetically separable property, Mater. Res. Bull. 104 (2018) 124−133.

[26] M.E. Lamm, K. Li, J. Qian, L. Wang, N. Lavoine, R. Newman, D.J. Gardner, T. Li, L. B. Hu, A.J. Ragauskas, Recent advances in functional materials through cellulose nanofiber templating, Adv. Mater. 33 (2021) 2005538.

[27] K.S. Ogueri, C.T. Laurencin, Nanofiber technology for regenerative engineering, ACS Nano 8 (2020) 9347−9363.

[28] L. Xu, B. Dong, Y. Wang, X. Bai, Q. Liu, H.W. Song, Electrospinning preparation and room temperature gas sensing properties of porous In_2O_3 nanotubes and nanowires, Sensor. Actuator. B Chem. 147 (2010) 531−538.

[29] S. Li, S. Zhou, H. Xu, L. Xiao, Y. Wang, H. Shen, H. Wang, Q. Yuan, Luminescent properties and sensing performance of a carbon quantum dot encapsulated mesoporous silica/polyacrylonitrile electrospun nanofibrous membrane, J. Mater. Sci. 51 (2016) 6801−6811.

[30] S. Yang, C.L. Shao, X.J. Zhou, X.H. Li, R. Tao, X.W. Li, S. Liu, Y.C. Liu, $MoSe_2$/TiO_2 nanofibers for cycling photocatalytic removing water pollutants under UV-Vis-NIR Light, ACS. Nano Mater. 3 (2020) 2278−2287.

[31] X.H. Yang, L. Li, L.B. Yuan, S.Z. Li, S.Z. Luo, Y.X. Liu, L.R. Peng, Submicrometer organic silica gel fiber for oxygen sensing, Opt. Lett. 36 (2011) 4656−4658.

[32] T.T. Yuan, X.X. Qi, Z.H. Liu, J. Yang, C.Y. Guan, Q.L. Long, J.M. Cao, M. Luo, X. H. Yang, L.B. Yuan, Humidity sensor based on micro optical fiber array fabricated by electrospinning, Opt Commun. 427 (2018) 517−521.

[33] V.O. Odhiambo, C.R.M. Mustafa, L.B. Thong, Z. Kónya, I.M. Szilágyi, Preparation of TiO_2/WO_3/C/N composite nanofibers by electrospinning using precursors soluble in water and their photocatalytic activity in visible light, Nanomaterials 11 (2021) 351.

[34] R.R. Nath, C. Nethravathi, M. rahamathi, Hierarchically porous, biphasic, and C-doped TiO_2 for solar photocatalytic degradation of dyes and selective oxidation of benzyl alcohol, ACS Omega 6 (2021) 12124−12132.

[35] L. Zhang, H. Wang, Z. Chen, P.K. Wong, J. Liu, Bi_2WO_6 micro/nano-structures: synthesis, modifications and visible-light-driven photocatalytic applications, Appl. Catal. B Environ. 106 (2011) 1−13.

[36] F. Wang, H. Yang, Y. Zhang, Enhanced photocatalytic performance of $CuBi_2O_4$ particles decorated with Ag nanowires, Mater. Sci. Semicond. Process. 73 (2018) 58−66.

[37] Y. Nakabayashi, Y. Nishikawa, Y. Nosaka, Fabrication of $CuBi_2O_4$ photocathode through novel anodic electrodeposition for solar hydrogen production, Electrochim. Acta 125 (2014) 191−198.

[38] A. Phuruangrat, P. Dumrongrojthanath, S. Thongtem, T. Thongtem, Hydrothermal synthesis of I-doped Bi_2WO_6 for using as a visible-light-driven photocatalyst, Mater. Lett. 224 (2018) 67−70.

[39] F. Yang, X.J. Yu, Z.B. Liu, J.F. Niu, T. Zhang, J.K. Nie, N.N. Zhao, J.P. Li, B.H. Yao, Preparation of Z-scheme $CuBi_2O_4$/Bi_2O_3 nanocomposites using, electrospinning and their enhanced photocatalytic performance, Mater. Today Commu. (2021) 101735.

[40] G. Venkatesha, S. Prabhub, M. Geerthanab, P. Baskaranc, R. Rameshb, K. M. Prabua, Facile synthesis of rGO/$CaSnO_3$ nanocomposite as an efficient photocatalyst for the degradation of organic dye, Optik 212 (2020) 164716.

[41] X. Zhang, C. Shao, X. Li, N. Lu, K. Wang, F. Miao, Y. Liu, In_2S_3/carbon nanofibers/Au ternary synergetic system: hierarchical assembly and enhanced visible-light photocatalytic activity, J. Hazard Mater. 283 (2015) 599−607.